



# Visualizing the double-gyroid twin

Xueyan Feng<sup>a</sup>, Mujin Zhuo<sup>b</sup>, Hua Guo<sup>b</sup>, and Edwin L. Thomas<sup>a,1</sup>

<sup>a</sup>Department of Materials Science and Engineering, Texas A&M University, College Station, TX 77840; and <sup>b</sup>Department of Material Science and Nano Engineering, Rice University, Houston, TX 77005

Edited by Frank S. Bates, University of Minnesota, Minneapolis, MN, and approved February 4, 2021 (received for review September 8, 2020)

**Periodic gyroid network materials have many interesting properties (band gaps, topologically protected modes, superior charge and mass transport, and outstanding mechanical properties) due to the space-group symmetries and their multichannel triply continuous morphology. The three-dimensional structure of a twin boundary in a self-assembled polystyrene-*b*-polydimethylsiloxane (PS-PDMS) double-gyroid (DG) forming diblock copolymer is directly visualized using dual-beam scanning microscopy. The reconstruction clearly shows that the intermaterial dividing surface (IMDS) is smooth and continuous across the boundary plane as the pairs of chiral PDMS networks suddenly change their handedness. The boundary plane therefore acts as a topological mirror. The morphology of the normally chiral nodes and strut loops within the networks is altered in the twin-boundary plane with the formation of three new types of achiral nodes and the appearance of two new classes of achiral loops. The boundary region shares a very similar surface/volume ratio and distribution of the mean and Gaussian curvatures of the IMDS as the adjacent ordered DG grain regions, suggesting the twin is a low-energy boundary.**

twin boundary | bicontinuous tubular network structure | 3D tomography | self-assembly | block copolymer

**S**upramolecular crystals are hierarchical assemblies possessing unique combinations of symmetries, feature sizes, and component compositions, all of which contribute to the expression of their unique properties (1, 2). Imperfections of various types can be introduced during molecular ordering. Investigating defects appearing within supramolecular crystals is an important endeavor to enable deeper understanding of their influence on properties and to improve material performance by eliminating or manipulating defects for beneficial effects (3).

Grain boundaries are the surface regions between ordered domains having different symmetry and/or orientation (4). Grain boundaries disrupt the continuous expression of symmetry, and impact many types of properties. Among the different classes of grain boundaries, the twin boundary (TB) is special due to its low energy and therefore wide occurrence. TBs are well studied in hard crystals and often appear during crystal growth or by the application of mechanical forces to an untwined crystal. TBs that form reentrant growth faces are important for accelerating crystal growth (5) and the presence of twins can strongly influence mechanical behavior (6). The unique character of the bonding in the TBs can also influence for example, electrical (7) and optical (8) properties. Twin structures can be constructed via the symmetry operations of reflection, rotation, or inversion (9). For crystals, where atom positions can be precisely identified using atom-resolved electron microscopy and computed via first-principles atomistic calculations, a very large number of detailed investigations on the precise nature of TBs have been made for various material classes, including metals (10, 11) and their alloys (12, 13), ceramics (14), small organic molecules (15), polymer crystals (16), protein crystals (17), and shell biomineralization (18). For colloidal crystalline systems with much larger “atoms” (micrometer-sized colloidal particles), twinning is also well studied (19, 20). Beyond the materials community, twinning also attracts interest from the fields of geometric crystallography (9, 21) and statistical analysis (22). However, to date, the investigation of TBs in soft-matter supramolecular

crystals has been rather limited. Unlike a hard crystal such as iron, having two atoms per body-centered cubic unit cell with a lattice parameter of a fraction of 1 nm, the typical unit cell of a supramolecular crystal would comprise tens of thousands of molecules and millions of atoms with a unit-cell edge of upwards of ~100 nm. The periodicity of such a soft-matter supramolecular crystal arises not from having the various types of atoms occupy precise positions within the unit cell, but rather allowing considerable positional freedom of the atoms and indeed of the molecules by only restricting certain portions of a molecule to lie within and uniformly fill the continuous periodic partitioning surfaces (also called the intermaterial dividing surface—IMDS) (23).

Structures based on Schoen’s gyroid (G) triply periodic minimal surface (TPMS) (24) are widely observed in many different soft-matter systems, including liquid crystals (25), surfactants (26), block copolymers (BCP) (27), and even butterfly wings (28, 29). The skeletal network of the triply periodic tubular network structure has the same geometry and topology as the (10, 3)-a graph defined by Wells (30). We employ a similar 10–3<sup>10</sup> notation to indicate the smallest closed loop in this network, consisting of 10 nodes with each node having three neighbors. The double-gyroid (DG) structure (31) consists of two independent, opposite-handed, interpenetrating (10, 3)-a networks. Within each network, every node is connected to three adjacent nodes. For the BCP DG structure, the minority block occupies the space surrounding the two network graphs and the majority block surrounds the minority block, infilling the region between the G TPMS and the two IMDSs. There are 16 equivalent node positions in the DG unit cell [space group *Ia*3̄*d* with nodes at Wyckoff site 16b having site symmetry (32)]. The basic chiral node motif occupying the Wyckoff site is a tripodal

## Significance

**The characterization of periodic morphologies in soft-matter supramolecular crystals has generally relied on X-ray scattering and transmission electron microscopy techniques. However, understanding the detailed nature of geometrical and topological defects in complex supramolecular assemblies requires high-resolution three-dimensional visualization over large sample volumes. Taking advantage of the recent development of slice-and-view scanning electron microscopy tomography for block copolymers, we clearly identify a sharp, coherent grain boundary in a double-gyroid structured polystyrene-*b*-polydimethylsiloxane diblock as a (422) twin boundary, likely formed during self-assembly. Knowledge of the geometric and topological nature of defects is important for further improving the performance of supramolecular soft crystals.**

Author contributions: X.F., M.Z., and E.L.T. designed research; X.F., M.Z., and H.G. performed research; X.F., H.G., and E.L.T. analyzed data; and X.F. and E.L.T. wrote the paper.

The authors declare no competing interest.

This article is a PNAS Direct Submission.

This open access article is distributed under [Creative Commons Attribution-NonCommercial-NoDerivatives License 4.0 \(CC BY-NC-ND\)](https://creativecommons.org/licenses/by-nc-nd/4.0/).

<sup>1</sup>To whom correspondence may be addressed. Email: elt@tamu.edu.

This article contains supporting information online at <https://www.pnas.org/lookup/suppl/doi:10.1073/pnas.2018977118/-DCSupplemental>.

Published March 15, 2021.

minority component domain, surrounded by the outer majority component domain. The IMDS separates the two components and exhibits a shape which can be approximated by constant mean-curvature variants of the Schoen's G surface (32, 33). Unlike traditional atomic crystals where the structure can be described by assigning the discrete atoms to specific Wyckoff sites in the unit cell, the crystalline order of the DG structure lies with the three-dimensional (3D) shape of the IMDS and the positions of the interconnected nodes. Along the ideal network graph, the dihedral angle between planes containing adjacent three coplanar struts rotates by  $\pm 70.5^\circ$  ("+" for clockwise [CW] and "-" for counterclockwise [CCW]) defining the network chirality (right- and left-handed, respectively). The  $Ia\bar{3}d$  space group includes inversion centers, two- and threefold rotational axes, and two-, three-, and fourfold screw axes as well as numerous axial and diagonal glide planes, but does not have mirror symmetry.

Materials comprising gyroid networks have been demonstrated to have many unique properties exploiting their particular symmetries for wave interactions as well as taking advantage of their triply continuous multichannel morphologies enabling superior charge or mass transport along with the possibility of outstanding mechanical properties due to the 3D continuity of a glassy component block (31). Example properties include a large complete photonic band gap for the single-gyroid network (34, 35), Weyl points in the band structure (36, 37), strong circular dichroic optical metamaterials (38), gas separation membranes (39, 40), advanced energy storage devices (i.e., the "gyroidal battery") (41), and optimized ionic conductors (42).

The appearance and detailed structural nature of TBs in soft-matter supramolecular gyroid crystals and their likely influence on the geometry, topology, and properties of the networks, has only recently been addressed. Two experimental studies and one mathematical modeling study mentioned TBs in DG. Vignolini et al. (43) briefly noted in 2012 what appeared to be some type of TB in a two-dimensional (2D) scanning electron microscopy (SEM) image of a surface region in their study of a metal network optical metamaterial fabricated from a BCP precursor template. In 2019, Chen (44) addressed the mathematical existence of twins in TPMSs including Schoen's G surface, and proposed a near-minimal surface model of the shape of a  $\{211\}$  G-surface twin. In 2020, Han et al. (45) proposed a  $(211) + 0.5$  G TB [which is equivalent to the  $(422)$  twin that we study] for a mesoporous silica-air sample based on a single transmission electron microscopy (TEM) image and matching this image to a series of projected models of the twin structure (for more discussion see *SI Appendix, Previous Studies*). To date, clear 3D visualization of the detailed features of a TB in a chiral DG network structure has yet to be achieved. Here, we employ slice-and-view SEM (SVSEM) tomography (46, 47) to study a TB structure in a self-assembled polystyrene-*b*-polydimethylsiloxane (PS-PDMS) soft-matter supramolecular crystal. High-fidelity 3D visualization of the TB is measured at both the supraunit-cell level and subunit-cell level. The boundary region shares similar surface/volume ratio and mean and Gaussian curvatures of the IMDS as for the adjacent ordered DG grain regions, suggesting the twin is a low-energy boundary. Furthermore, we clearly characterize the geometric and topological features of the node positions and node functionality of the TB and how they interconnect to the adjacent DG network neighborhood.

## Results and Discussion

During our ongoing investigation of grain boundaries in tubular BCP network phases, where the boundaries often appear as transitional aperiodic regions of substantial thickness, on the order of the length of several crystallographic unit cells, we encountered a sharp transitional region between adjacent 2D periodic surface patterns of a PS-PDMS DG sample (Fig. 1A). The PDMS domains appear bright in the secondary electron SEM image due to the

stronger scattering from the higher atomic number Si atoms and the darker regions correspond to the majority PS matrix. The surface image patterns in grain 1 and grain 2 are distinctly different and meet along a well-defined linear boundary (dashed yellow line), suggesting some type of special grain boundary. A tomogram from the 3D volume containing both grain 1 and grain 2 was created by obtaining a series of secondary electron images taken after removing each thin parallel slice by focused ion-beam (FIB) milling (Fig. 1B) (48). Based on segregation of the 3D SEM voxel intensity data, the PDMS and PS domains can be easily identified. The two independent PDMS networks are rendered in red and blue color for right-handed and left-handed network, respectively, with the PS matrix transparent (Fig. 1C). The data analysis software allows new, software-based, slice images of the 3D SEM voxel intensity data to be taken in the direction normal to the boundary plane. The resultant series of slice images is remarkably similar to the series of model images of the surface after each thin slice along the  $[211]$  direction of a DG level-set model having a minority network volume fraction of 0.40 (*SI Appendix, Fig. S1 and Movie S1*). Detailed inspection of individual images taken parallel to the sharp boundary plane definitively determines the boundary plane is a DG  $(422)$  plane (Fig. 1D).

Because of the coherence of the unit cells within a particular grain, the DG unit-cell parameters can be precisely measured based on 3D fast Fourier transformation (FFT) patterns (*SI Appendix, Fig. S2*). The single-grain pattern for each grain is

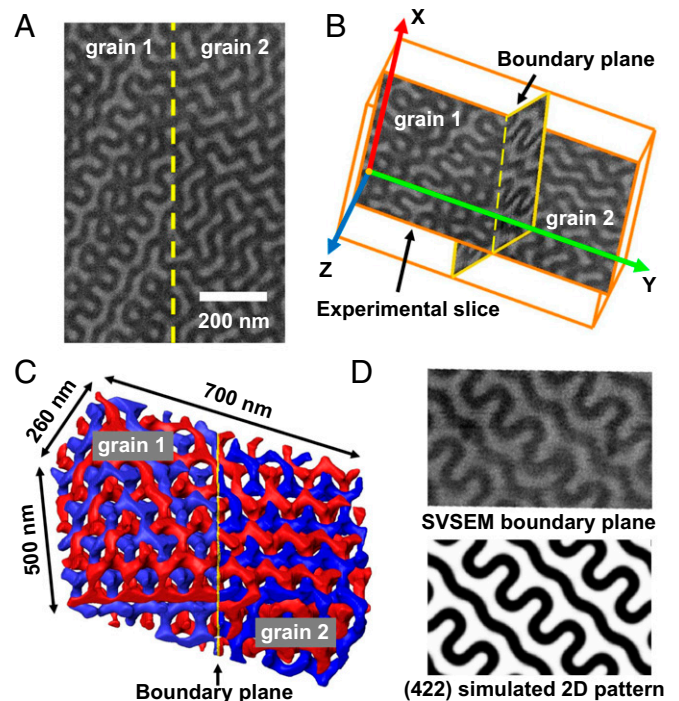


**Fig. 1. Sharp grain boundary.** (A) SEM image showing a region where two DG grains having distinct 2D intensity patterns (marked as grain 1 and grain 2) merge along a sharp line (yellow dashed line). PDMS domains are bright and the PS matrix is dark. (B) Perspective view of the 3D data volume with boundary plane identified. The laboratory coordinate frame is indicated, where the experimental 2D SEM images collected are parallel with X-Y plane and the FIB slicing direction is along Z. (C) A 3D experimental reconstruction of the boundary region volume containing two independent PDMS networks (rendered in color) embedded in the PS matrix (transparent). The sharp grain-boundary plane is highlighted in yellow. (D) Software-based slice image of the boundary plane from 3D SEM data along with the simulated 2D DG  $(422)$  pattern.

based on ~15 unit cells while that for the pattern for TB volume containing both grain 1 and grain 2 is based on ~44 unit cells. As noted in our previous work (46) as well as mentioned in studies on other solution-cast BCP systems (49–51), due to shrinkage stresses from solvent evaporation, the cubic unit cell is distorted into variants of a triclinic cell. The characteristic cell parameters ( $a, b, c, \alpha, \beta, \gamma$ ) for grain 1 and 2 are given in *SI Appendix, Table S1* with left-handed coordinates for grain 1 and right-handed coordinates for grain 2. The reconstruction shows that the chiral networks are continuous from grain 1 into grain 2 and suddenly change their handedness as they cross the boundary plane (*SI Appendix, Fig. S3*). The boundary plane therefore acts as a topological mirror (that is, the red [right-handed] and blue [left-handed] networks of grain 1 abruptly and smoothly transform to the blue [left-handed] and red [right-handed] networks of grain 2, respectively) (for further details see *SI Appendix, Network Dihedral Angle and Mirror Coherency of Two Grains*). Before further analysis of the TB, we construct a simple TB model based on the cubic level-set DG model for two minority component networks, each at 20 vol. %, employing a (422) plane as the TB. To create the model, a DG structure (volume 1) is made to have a terminating (422) surface plane. Then volume 2 is generated from volume 1 using the (422) surface plane as a mirror. Subsequent fusion is done by superposition of the terminating (422) surface planes of both volumes to yield the (unrelaxed) model twin structure (see *SI Appendix, Level Set (422) DG TB Model* for additional discussion of the construction and limitations of the level set model).

Side by side  $[1\bar{1}\bar{1}]$  and  $[01\bar{1}]$  views of the SVSEM reconstruction and of the model show excellent correspondence between the network morphology features of the experimental reconstruction and those of the level-set model (Fig. 2A and *SI Appendix, Fig. S4*; also see rotational videos in *Movie S2*). Due to the different geometrical distortions of the two grains from cubic symmetry by solvent shrinkage forces, the exact structural mirror symmetry between grain 1 and grain 2 is reduced; however, there is still strong mirror coherency (e.g., the handedness transition of networks when each network crosses the boundary plane, and good alignment between the same symmetry directions of grain 1 and grain 2) as further discussed in *SI Appendix, Mirror Coherency of Two Grains*.

The (422) TB creates changes in the shape of the IMDS and the interconnections of the nodes within the boundary neighborhood. For reference, in the ideal DG crystal, all nodes have three struts ( $f = 3$ ) and are located at Wyckoff site 16b. The (422) plane has two sets of equivalent locations of  $f = 3$  DG nodes within both the right-handed and left-handed networks, respectively (marked as *i* and *ii* and colored red and blue for nodes in the right-handed and left-handed networks, respectively; see model pattern at the top part of Fig. 2D). In the (422) TB region, three new types of boundary nodes are created which can be observed in both the SVSEM reconstruction and in the model (Fig. 2B–D): type 1 with  $f = 3$  (green), type 2 with  $f = 3$  (yellow), and type 3 with  $f = 4$  (aqua). By analyzing the model, the origin of boundary nodes is clear. Type 1 and 2 nodes can be thought of as being created by fusion of two half in-plane  $f = 3$  DG nodes at the mirror plane, one-half from the red (right-handed) and one-half from the blue (left-handed) network, respectively. These mirror symmetric  $f = 3$  boundary nodes occupy the original positions of the corresponding in-plane  $f = 3$  DG nodes. The type-3  $f = 4$  nodes may be envisioned as the inward displacement and fusion of two out-of-plane  $f = 3$  DG nodes (Fig. 2B and *SI Appendix, Fig. S5*). In the regions adjacent to the TB, all nodes are the regular  $f = 3$  DG nodes. The three types of boundary nodes introduce new dihedral angles and internode distances as shown in *SI Appendix, Figs. S6 and S7* and discussed in *SI Appendix, Network Dihedral Angle and Length of TB Struts*. The CW and

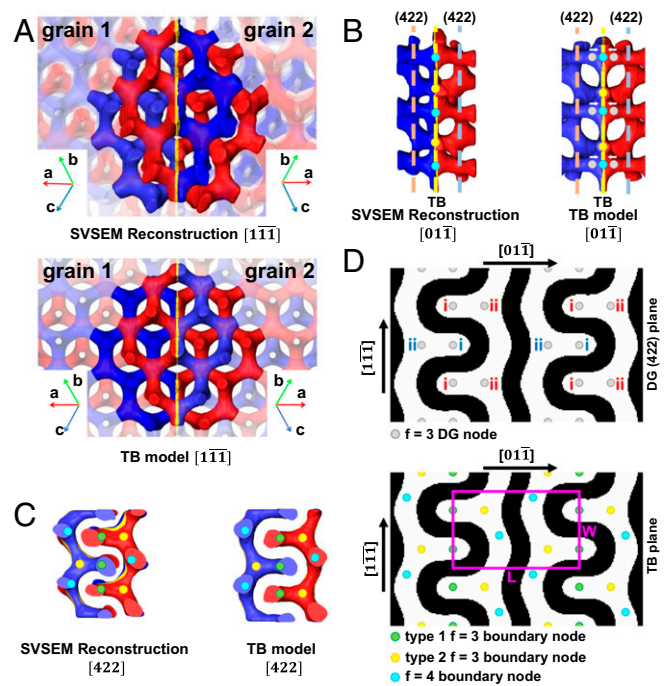


**Fig. 2.** The (422) TB structure. (A) SVSEM experimental reconstruction of the interpenetrating PDMS networks near the TB (Top) and level-set model (Bottom) viewed along the  $[1\bar{1}\bar{1}]$  direction showing good correspondence with mirror symmetry across the boundary. The highlighted partial reconstruction and model are both embedded within surrounding translucent networks. (B and C) SVSEM reconstruction (Left) and model (Right) of partial networks viewed along the  $[01\bar{1}]$  and  $[422]$  directions showing different types of boundary nodes. Only one of the two networks is shown in B for clearer visualization of the nodes. The locations of different types of nodes are labeled with colored dots: gray for regular  $f = 3$  DG nodes, green for type 1  $f = 3$  boundary nodes, yellow for type 2  $f = 3$  boundary nodes, and aqua for type 3  $f = 4$  boundary nodes. (D) The (422) plane from level-set model with different node-type positions labeled. At the top part, the DG (422) plane with regular DG nodes (gray) are indicated. Two sets of equivalent locations of  $f = 3$  DG nodes within both right-handed (red) and left-handed (blue) networks are labeled as “*i*” and “*ii*.” At the bottom part, the pattern shows three types of nodes for the (422) TB plane. One TB 2D unit cell within the boundary plane is indicated by purple rectangle having the length ( $L$ ) of  $\sqrt{2}a$  and width ( $W$ ) of  $\sqrt{3}a$ , where  $a$  is the cubic DG unit cell length. This 2D unit cell is bounded by two  $(1\bar{1}\bar{1})$  planes and two  $(02\bar{2})$  planes.

CCW dihedral angles always appear in pairs, consistent with the intrinsic achiral nature of the TB.

The morphology of the basic loops within the networks near the boundary is also altered. Recall the shortest closed path in a gyroid network is the  $10\text{--}3^{10}$  loop (a path of 10 equal size steps between adjacent  $f = 3$  nodes; such loops can be either right- or left-handed) (47). The occurrence of a TB enriches the set of loops, which can be grouped into two classes (Fig. 3). In one class, the boundary plane bisects the loop leading to three types of mirror symmetric loops. One is a new type of  $10\text{--}3^{10}$  loop different from the basic asymmetric  $10\text{--}3^{10}$  loop. Another type, named  $10\text{--}4$ ,  $3^9$  has a single  $f = 4$  node and nine  $f = 3$  nodes, and the third loop type is named  $8\text{--}4$ ,  $3^7$  comprising an  $f = 4$  node and seven  $f = 3$  nodes. The second class of loops consists of mirror-symmetric, fused loop pairs with the TB plane bisecting the fused struts common to both loops. There are six members in this class indexed as:  $U2\text{--}9\text{--}4,3,4,3^6$ ;  $U2\text{--}9\text{--}4,3^8$ ;  $U2\text{--}10\text{--}4,3^9$ ;  $U2\text{--}9\text{--}4,3,4,3^6$ ;  $U2\text{--}10\text{--}4,3^9$ ; and  $U2\text{--}9\text{--}4,3^8$  (here,  $U2$  means the union of two loops).

Close inspection of the experimental data shows some departures from the model structure primarily from geometrical distortions of the networks from solvent shrinkage forces.

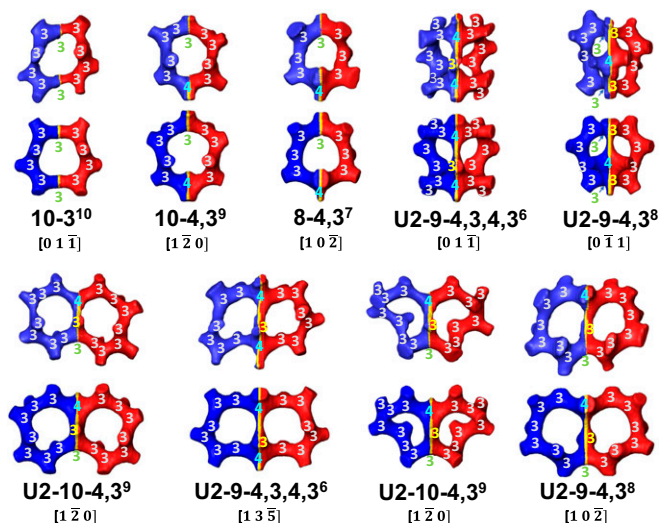


**Fig. 3.** Classifying loops within the TB neighborhood. Images of experimental SVSEM loops (rows 1 and 3) and their corresponding level-set models (rows 2 and 4). The loops can be placed into two classes: one class contains three members (upper-left set) with the TB plane bisecting each loop; the second class (denoted as U2, meaning union of two loops) contains six members with pairs of loops fusing together at the twin plane. Node functionality and type is delineated by colored numbers. Gray for the regular  $f = 3$  DG nodes, green for type-1  $f = 3$  boundary nodes, yellow for type-2  $f = 3$  boundary nodes, and aqua for type-3  $f = 4$  boundary nodes. The experimental loops show some distortions, but all experimental loops match up well with their corresponding model. The notation  $X-Y^n$  is used to describe the various loops, where  $X$  = total number of nodes in the loop with functionality  $Y$ , repeated  $n$  times.

However, specific characteristic geometrical and topological features (such as boundary nodes, boundary loops) correspond quite well between experimental reconstruction and TB model as shown in Figs. 2 and 3 and *SI Appendix, Fig. S5*. The introduction of new types and sizes of loops along with new types of nodes in the TB changes the local topology which can influence properties (52, 53). One approach to quantify the topology is to evaluate the Euler characteristic of the IMDS within a volume containing the TB and comparing to an identical volume in the ordered DG. However, due to the occasional presence of network break defects, as well as the influence of the particular choices of faces of the cutting planes

defining each volume (54), along with small shifts in the relative locations of the planar cuts with respect to the nodes due to the variable shrinkage distortions, such evaluation is beyond the scope of the current paper.

The detailed shape of the IMDS reflects the molecular packing within the self-assembled phase. The mean ( $H$ ) and Gaussian ( $K$ ) curvature distributions of the reconstructed IMDS were measured for the TB neighborhood volume as well as corresponding ordered DG volumes in the adjacent grains (the three volumes are shown in *SI Appendix, Fig. S8 A–C* and see *SI Appendix, Cropped Volume for IMDS Analysis*). The distribution of the dimensionless  $H$  and  $K$  values over the IMDS of the three volumes, normalized by  $\langle D \rangle = 130$  nm (the average lattice parameter cell dimension measured by small angle X-ray scattering [SAXS]), are plotted in Fig. 4 A–C. The curvatures of two limiting theoretical IMDS shapes, the constant matrix thickness (CMT) surface and the constant mean curvature (CMC) surface, are also plotted for reference (diagonal line for CMT and vertical line for CMC). The CMT surface, which is a parallel surface, displaced a constant distance along the local normal from the G minimal surface, can minimize the entropic penalty of variable stretching of the majority component chains at the expense of slight increase in interfacial area of the IMDS, while a CMC surface minimizes the area of the IMDS at a fixed volume fraction (46). As shown in Fig. 4 A–C, the curvature probability distributions of the BCP IMDS for the TB volume and corresponding DG volumes are very similar. Also, the surface/volume ratios of the PDMS networks in the three volumes are quite similar, varying from  $0.115$  to  $0.116$  nm<sup>-1</sup>. The strong resemblance of these various IMDS features suggest the (422) TB is a relatively low-energy grain boundary.

There are three modes for twin formation: growth twins, phase transformation twins, and deformation twins. For this BCP DG sample cast from toluene solution at room temperature, modest deformation forces only appear toward the latter drying stages of solution casting, where the concentration of sample solution becomes higher than the vitrification concentration of the PS domain (55). This rules out any abrupt, coherent local change of chirality of the PDMS networks within PS matrix at room temperature by mechanical force. Also, SAXS observations following the concentration dependence of structural order in the PS-PDMS toluene solution at room temperature prove no order–order phase transition occurs (55) [e.g., hexagonally perforated layers to DG transition, which has been suggested to be likely related to the gyroidal TB (45)]. Instead, it is most likely that the (422) BCP DG twin is a growth twin, where nucleation can take place more easily at the concave reentrant grooves formed by low-energy

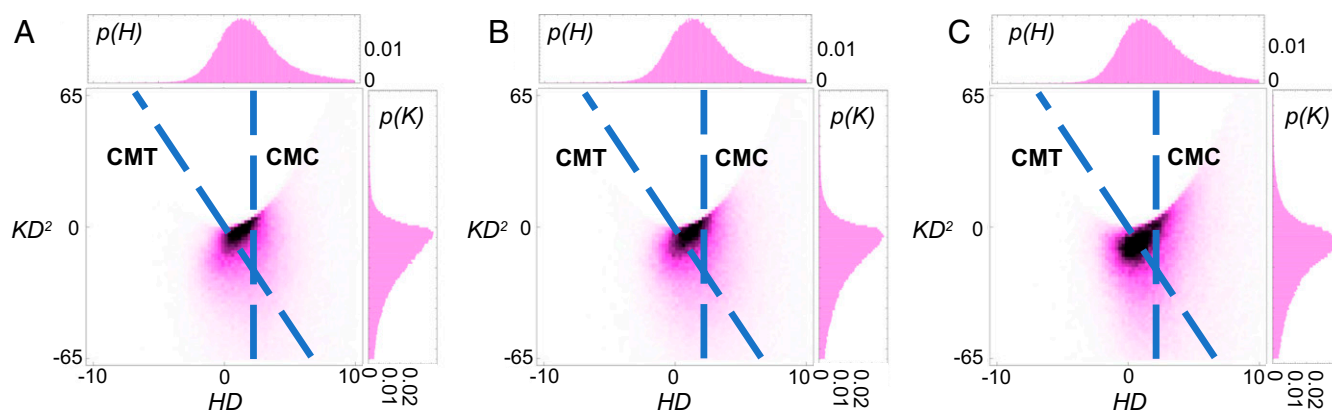


**Fig. 4.** IMDS. Normalized Gaussian ( $K$ ) and mean ( $H$ ) curvatures and their respective probability functions for the volumes of grain 1 region (A), TB region (B), and grain 2 region (C); three volumes are shown in *SI Appendix, Fig. S8 A–C*. The curvatures are normalized by  $\langle D \rangle = 130$  nm. The diagonal ( $HD = -0.103 KD^2$ ) and vertical ( $HD = 2.23$ ) dashed blue lines indicate the curvature distributions for a constant minimal G surface thickness (CMT) IMDS and a constant mean-curvature (CMC) IMDS of cubic DG with a minority volume fraction of 40% (46).

growth faces of a twinned crystal (5). A more detailed understanding of the structural evolution of twin formation in self-assembled BCPs requires further in situ experiments.

## Concluding Remarks

A sharp, coherent grain boundary in a PS-PDMS diblock with the DG phase has been shown to be a (422) TB, likely formed during self-assembly of the growing crystal. The twin creates a mirror relationship between neighboring DG grains, resulting in a smooth but abrupt topological mirror transformation of the two enantiomorphic pairs of gyroid networks across the boundary. Three new types of network nodes along with nine new network loops and their corresponding dihedral angles are identified and described. The surface/volume ratio and mean and Gaussian curvatures of the IMDS in the boundary region volume are all very similar to the same morphological characteristics measured in the adjacent DG grains, suggesting that the TB is of low energy. This clear elucidation of the 3D detailed structure of a twin in a BCP DG structure has important implications for the occurrence of crystallographic internal surface defects in tubular phases and their influence on the properties of soft-matter phases where, despite the complex topology of the network domain and interpenetration of multiple networks, low-energy planar defects can occur.

## Materials and Methods

**Material and Sample Preparation.** The PS-PDMS diblock copolymer was synthesized by sequential anionic polymerization of styrene and hexamethylcyclotrisiloxane as reported in ref. 55. The number average molecular weights of the PS block and the PDMS block are 43.5 and 29.0 kg/mol, respectively. The volume fraction of PDMS block is ~40% and dispersity for the whole PS-PDMS polymer is 1.04. The sample studied was slowly cast over 1 wk from a 10 wt. % solution (2 mL) in toluene. After drying, the sample was heated to 60° C for 3 d with vacuum in order to remove any residual solvent. The sample was characterized by synchrotron X-ray at Sector 12-ID-B of Advanced Photon Source in Argonne National Laboratory before study by SVSEM. Based on the SAXS pattern, the structure can be nominally associated with a DG morphology, with an average cubic repeat of  $\langle D \rangle = 130$  nm (46). Forbidden reflections for the cubic  $Ia\bar{3}d$  space group are observed, suggesting nonaffine deformation of DG unit cells. Before SVSEM imaging, the sample was attached to a 45° SEM stub with double-sided conductive carbon tape; and the outer surface was then coated with a 50-nm layer of platinum.

**SVSEM Data.** The acquisition of SVSEM data follows the procedure reported in ref. 46. A Thermo Fisher Helios NanoLab 660 SEM-FIB DualBeam system using a gallium ion beam ( $\text{Ga}^+$ ) having an energy of 30 keV with a current of 80 pA was used to mill the sample surface. A 2-keV electron beam with beam current of 50 pA was used to image the sample surface with a Through Lens (TLD) secondary electron (SE) detector. Notably, the stronger scattering from the higher atomic number of Si atoms in the PDMS and the resulting additional SE emission is sufficient to provide excellent intrinsic contrast between the PS and PDMS domains without staining. Fiducials were used to register the FIB and SE images during the automatic SV process. The pixel resolution for each 2D SEM image collected is 1.37 nm per pixel. The actual FIB slice thicknesses during the image acquisition process were monitored based on FIB images as  $4.61 \pm 0.04$  nm per slice (for details see *SI Appendix*, Fig. S9).

**Data Processing and Analysis.** ImageJ (<https://imagej.nih.gov/ij/>) was used to binarize the grayscale image stack data to identify the tubular networks formed by the minority domains and separated them from the majority block-filled matrix by using a threshold such that the volume fractions of the two binary components matched with the experimentally reported block volume fraction (~40%). Reconstructions and morphological analysis were

done with Avizo software from Thermo Fisher and Supporting Software reported in ref. 46. The supporting software can be found on the online data repository at <https://scholarworks.umass.edu/data/88/>.

**Three-dimensional FFT analysis of grains.** The coherence of the unit cells within a DG grain enables high-resolution analysis of 3D SVSEM data set in reciprocal space, extracting the unit-cell vector information. Before transforming the real-space volume data into Fourier space, a Hanning window was applied on the raw SEM data volume in order to reduce artifacts in the FFT associated with sample boundary discontinuities. The unit-cell vectors of the DG structure can be obtained from the indexed 3D FFT pattern.

**Three-dimensional reconstruction.** Based on the binarized images, a 3D volume can be reconstructed as colored PDMS networks within a transparent PS matrix using Avizo software from Thermo Fisher. Subvolumes of regions of interest can be further cropped out for local analysis. The area of PDMS network surface (i.e., IMDS) and the volume of PDMS networks can be measured with the integrated function in Avizo for the calculation of surface/volume ratio of PDMS networks.

**Dihedral angle analysis of networks.** Dihedral angle analysis is based on the skeletal graph of PDMS networks. We extracted the skeleton directly from the binarized 3D volume with the *skeletonization* feature in ImageJ (<https://imagej.nih.gov/ij/>). The skeleton data were imported into the Supporting Information software for the measurement of dihedral angles (Supporting Information software can be found on the online data repository at <https://scholarworks.umass.edu/data/88/>). For a given triplet of consecutive struts within the skeleton, we defined the two planes and their normal as  $\hat{n}_{\alpha\beta} = (\hat{r}_\alpha \times \hat{r}_\beta) / |(\hat{r}_\alpha \times \hat{r}_\beta)|$  and  $\hat{n}_{\beta\gamma} = (\hat{r}_\beta \times \hat{r}_\gamma) / |(\hat{r}_\beta \times \hat{r}_\gamma)|$ , where  $\hat{r}_\alpha$ ,  $\hat{r}_\beta$ , and  $\hat{r}_\gamma$  are the unit vectors along the struts. The dihedral angle is defined as the angle between these plane normals, with  $\sin\theta = (\hat{n}_{\alpha\beta} \times \hat{n}_{\beta\gamma}) \cdot \hat{r}_\beta$ ,  $\cos\theta = \hat{n}_{\alpha\beta} \cdot \hat{n}_{\beta\gamma}$ .

**Curvature calculation.** The curvature measurement of IMDS was done by supporting information software for the measurement of IMDS curvature (supporting information software can be found on the online data repository at <https://scholarworks.umass.edu/data/88/>). The IMDS is represented as a triangulated mesh which was identified by finding a surface of the linear interpolation of the 3D Gaussian-filtered binarized volume data at  $\phi_{40}$  which separated the 3D volume into PDMS domains (40% volume) and PS domains (60% volume). We further employed two-step conditioning to this mesh by 1) applying an edge-length regularization, and 2) constraining the mesh vertices to lie on the isosurface of a third-order interpolation of the density to ensure mesh vertices represent a surface that is at least second-order differentiable. The principal curvatures  $\kappa_1$  and  $\kappa_2$  associated with each triangulated vertex can be calculated by fitting a paraboloid to that vertex and its nearest neighbors, with the paraboloid axis constrained along the vertex normal. From the principal curvatures, the mean curvature  $H = \frac{(\kappa_1 + \kappa_2)}{2}$  and Gaussian curvature  $K = \kappa_1 \kappa_2$  are calculated for each vertex.

**Level-set model.** The model of the DG (422) twin TB was made using a level-set representation of the DG (56). The level-set equation used is

$$F(x, y, z) = \sin(2\pi x) \times \cos(2\pi y) + \sin(2\pi y) \times \cos(2\pi z) + \sin(2\pi z) \times \cos(2\pi x) = t.$$

By setting  $t$  to 0.91, the volume fraction of the minority networks is ~40%. The surface file written by the level-set equation was introduced into Avizo software and the surface was converted into solid network volume and further sliced into 2D image stack for the construction of TB model.

**Data Availability.** The SVSEM data and image files have been deposited in Texas Data Repository and are available at <https://dataverse.tdl.org/dataset.xhtml?persistentId=doi:10.18738/T8/TIO8WJ>. All other study data are included in the article and/or supporting information.

**ACKNOWLEDGMENTS.** This research was support by a grant from the NSF under Award DMR 1742864. We thank C. J. Burke, A. Reddy, and G. M. Grason from University of Massachusetts for the development of morphology analysis codes. We thank B. van Leer, T. Lacon, and T. Santisteban from Thermo Fisher for helpful insights on hardware and software for SVSEM tomography.

1. S. Hyde *et al.*, *The Language of Shape 141-197* (Elsevier Science, 1997).
2. D. B. Amabilino, D. K. Smith, J. W. Steed, Supramolecular materials. *Chem. Soc. Rev.* **46**, 2404–2420 (2017).
3. S. Bai, N. Zhang, C. Gao, Y. J. Xiong, Defect engineering in photocatalytic materials. *Nano Energy* **53**, 296–336 (2018).
4. V. Randle, Grain boundary engineering: An overview after 25 years. *Mater. Sci. Technol.* **26**, 253–261 (2010).
5. A. J. Shahani, E. B. Gulsoy, S. O. Poulsen, X. Xiao, P. W. Voorhees, Twin-mediated crystal growth: An enigma resolved. *Sci. Rep.* **6**, 28651 (2016).

6. J. Y. Wu, S. Nagao, J. Y. He, Z. L. Zhang, Role of five-fold twin boundary on the enhanced mechanical properties of fcc Fe nanowires. *Nano Lett.* **11**, 5264–5273 (2011).
7. K. C. Kim *et al.*, Free-electron creation at the 60° twin boundary in Bi<sub>2</sub>Te<sub>3</sub>. *Nat. Commun.* **7**, 12449 (2016).
8. A. M. van der Zande *et al.*, Grains and grain boundaries in highly crystalline monolayer molybdenum disulphide. *Nat. Mater.* **12**, 554–561 (2013).
9. H. Grimmer, M. Nespolo, Geminography: The crystallography of twins. *Z. Kristallogr.* **221**, 28–50 (2006).

10. Y. M. Wang *et al.*, Defective twin boundaries in nanotwinned metals. *Nat. Mater.* **12**, 697–702 (2013).
11. M. Song *et al.*, Oriented attachment induces fivefold twins by forming and decomposing high-energy grain boundaries. *Science* **367**, 40–45 (2020).
12. P. J. E. Forsyth, R. King, G. J. Metcalfe, B. Chalmers, Grain boundaries in metals. *Nature* **158**, 875–876 (1946).
13. Q. Yu *et al.*, Strong crystal size effect on deformation twinning. *Nature* **463**, 335–338 (2010).
14. C. L. Jia, K. Urban, Atomic-resolution measurement of oxygen concentration in oxide materials. *Science* **303**, 2001–2004 (2004).
15. E. R. Engel, S. Takamizawa, Versatile ferroelastic deformability in an organic single crystal by twinning about a molecular zone axis. *Angew. Chem. Int. Ed. Engl.* **57**, 11888–11892 (2018).
16. L. Cartier, T. Okihara, B. Lotz, Triangular polymer single crystals: Stereocomplexes, twins, and frustrated structures. *Macromolecules* **30**, 6313–6322 (1997).
17. H. Luecke, H. T. Richter, J. K. Lanyi, Proton transfer pathways in bacteriorhodopsin at 2.3 angstrom resolution. *Science* **280**, 1934–1937 (1998).
18. V. Schoeppler *et al.*, Crystal growth kinetics as an architectural constraint on the evolution of molluscan shells. *Proc. Natl. Acad. Sci. U.S.A.* **116**, 20388–20397 (2019).
19. L. Wang, J. Lu, B. Liu, Metastable self-assembly of theta-shaped colloids and twinning of their crystal phases. *Angew. Chem. Int. Ed. Engl.* **58**, 16433–16438 (2019).
20. K. Zhao, T. G. Mason, Twinning of rhombic colloidal crystals. *J. Am. Chem. Soc.* **134**, 18125–18131 (2012).
21. A. Santoro, Characterization of twinning. *Acta Crystallogr. A* **30**, 224–231 (1974).
22. A. C. Terwisscha van Scheltinga, K. Valegård, J. Hajdu, I. Andersson, MIR phasing using merohedrally twinned crystals. *Acta Crystallogr. D Biol. Crystallogr.* **59**, 2017–2022 (2003).
23. E. L. Thomas, D. M. Anderson, C. S. Henkee, D. Hoffman, Periodic area-minimizing surfaces in block copolymers. *Nature* **334**, 598–601 (1988).
24. A. H. Schoen, *Infinite Periodic Minimal Surfaces without Self-Intersections* (NASA, 1970).
25. F. Liu, M. Prehm, X. Zeng, C. Tschierske, G. Ungar, Skeletal cubic, lamellar, and ribbon phases of bundled thermotropic bolapolyphiles. *J. Am. Chem. Soc.* **136**, 6846–6849 (2014).
26. V. Luzzati, P. A. Spegt, Polymorphism of lipids. *Nature* **215**, 701–704 (1967).
27. D. A. Hajduk *et al.*, The gyroid—A new equilibrium morphology in weakly segregated diblock copolymers. *Macromolecules* **27**, 4063–4075 (1994).
28. B. D. Wilts *et al.*, Butterfly gyroid nanostructures as a time-frozen glimpse of intracellular membrane development. *Sci. Adv.* **3**, e1603119 (2017).
29. B. Winter *et al.*, Coexistence of both gyroid chiralities in individual butterfly wing scales of *Callophrys rubi*. *Proc. Natl. Acad. Sci. U.S.A.* **112**, 12911–12916 (2015).
30. A. F. Wells, *Three Dimensional Nets and Polyhedra* (Wiley, 1977).
31. E. L. Thomas, Nanoscale 3D ordered polymer networks. *Sci. China Chem.* **61**, 25–32 (2018).
32. K. Grosse-Brauckmann, Triply periodic minimal and constant mean curvature surfaces. *Interface Focus* **2**, 582–588 (2012).
33. T. Oka, N. Ohta, S. T. Hyde, Polar-nonpolar interfaces of normal bicontinuous cubic phases in nonionic surfactant/water systems are parallel to the gyroid surface. *Langmuir* **36**, 8687–8694 (2020).
34. M. Maldovan, A. M. Urbas, N. Yufa, W. C. Carter, E. L. Thomas, Photonic properties of bicontinuous cubic microphases. *Phys. Rev. B Condens. Matter Mater. Phys.* **65**, 165123 (2002).
35. A. M. Urbas, M. Maldovan, P. DeRege, E. L. Thomas, Bicontinuous cubic block copolymer photonic crystals. *Adv. Mater.* **14**, 1850–1853 (2002).
36. L. Lu, L. Fu, J. D. Joannopoulos, M. Soljacic, Weyl points and line nodes in gyroid photonic crystals. *Nat. Photonics* **7**, 294–299 (2013).
37. M. Fruchart *et al.*, Soft self-assembly of Weyl materials for light and sound. *Proc. Natl. Acad. Sci. U.S.A.* **115**, E3655–E3664 (2018).
38. C. Kilchoer *et al.*, Strong circular dichroism in single gyroid optical metamaterials. *Adv. Opt. Mater.* **8**, 1902131 (2020).
39. T. A. Shefelbine *et al.*, Core-shell gyroid morphology in a poly(isoprene-block-styrene-block-dimethylsiloxane) triblock copolymer. *J. Am. Chem. Soc.* **121**, 8457–8465 (1999).
40. L. Li *et al.*, Gyroid nanoporous membranes with tunable permeability. *ACS Nano* **5**, 7754–7766 (2011).
41. J. G. Werner, G. G. Rodriguez-Calero, H. D. Abruna, U. Wiesner, Block copolymer derived 3-D interpenetrating multifunctional gyroidal nanohybrids for electrical energy storage. *Energy Environ. Sci.* **11**, 1261–1270 (2018).
42. L. Yan, C. Rank, S. Mecking, K. I. Winey, Gyroid and other ordered morphologies in single-ion conducting polymers and their impact on ion conductivity. *J. Am. Chem. Soc.* **142**, 857–866 (2020).
43. S. Vignolini *et al.*, A 3D optical metamaterial made by self-assembly. *Adv. Mater.* **24**, OP23–OP27 (2012).
44. H. Chen, Minimal twin surfaces. *Exp. Math.* **28**, 404–419 (2019).
45. L. Han *et al.*, Crystal twinning of bicontinuous cubic structures. *IUCr* **7**, 228–237 (2020).
46. X. Feng *et al.*, Seeing mesoatomic distortions in soft-matter crystals of a double-gyroid block copolymer. *Nature* **575**, 175–179 (2019).
47. X. Y. Feng, H. Guo, E. L. Thomas, Topological defects in tubular network block copolymers. *Polymer* **168**, 44–52 (2019).
48. X. Feng, M. Zhuo, H. Guo, E. L. Thomas, Raw data for "Visualizing the double gyroid twin." Texas Data Repository. <https://dataverse.tdl.org/dataset.xhtml?persistentId=doi:10.18738/T8/TIO8WJ>. Deposited 9 February 2021.
49. G. E. S. Toombes *et al.*, A re-evaluation of the morphology of a bicontinuous block copolymer-ceramic material. *Macromolecules* **40**, 8974–8982 (2007).
50. M. Faber, A. H. Hofman, K. Loos, G. T. Brinke, Highly ordered structure formation in RAFT-synthesized PtBOS-b-P4VP diblock copolymers. *Macromol. Rapid Commun.* **37**, 911–919 (2016).
51. J. A. Dolan *et al.*, Controlling self-assembly in gyroid terpolymer films by solvent vapor annealing. *Small* **14**, e1802401 (2018).
52. S. Gupta, A. Saxena, A topological twist on materials science. *MRS Bull.* **39**, 265–279 (2014).
53. L. Chico, V. H. Crespi, L. X. Benedict, S. G. Louie, M. L. Cohen, Pure carbon nanoscale devices: Nanotube heterojunctions. *Phys. Rev. Lett.* **76**, 971–974 (1996).
54. A. Odgaard, H. J. G. Gundersen, Quantification of connectivity in cancellous bone, with special emphasis on 3-D reconstructions. *Bone* **14**, 173–182 (1993).
55. T. Y. Lo *et al.*, Phase transitions of polystyrene-b-poly(dimethylsiloxane) in solvents of varying selectivity. *Macromolecules* **46**, 7513–7524 (2013).
56. M. Wohlgenuth, N. Yufa, J. Hoffman, E. L. Thomas, Triply periodic bicontinuous cubic microdomain morphologies by symmetries. *Macromolecules* **34**, 6083–6089 (2001).